MŰEGYETEM 1782

DEGREE WORK

Sándor Tóth

Electron spin resonance study of the $N@C_{60}$ encapsulated inside single-walled carbon nanotubes

Supervisor:

Dr. Ferenc Simon
associate professor
BUTE, Institute of Physics
Department of Experimental Physics

BUTE
2008

Köszönetnyilvánítás

Hálával tartozom szüleimnek, amiért felneveltek és minden lehetőséget megadtak arra, hogy a saját utamat kövessem. Apunak köszönhetem, hogy a gyermeki kíváncsiság még ma is megvan bennem. Köszönöm az egész családnak, hogy olyannak szeretnek amilyen vagyok még a végtelen feledékenységemmel együtt is. Köszönöm Zsófinak, hogy türlemes volt velem amíg dolgoztam. Köszönettel tartozom gimnáziumi fizikatanáromnak, Szucsán Andrásnak, aki rávezetett a fizika szépségére.

Hálával tartozom témavezetőmnek, Simon Ferencnek, azért hogy megmutatta miként lehet hatékonyan és eredményesen kutatni, mert megadta a kezdő lökést a sikeres tudományos pályához, és a snowboardozásért Kirchbergben. Legnagyobbrészt neki köszönhető hogy a dolgozatom legalább köszönőviszonyban van az angollal. Köszönetet mondok Jánossy Andrásnak, a Kísérleti Fizika Tanszék tanszékvezetőjének és a tanszék minden dolgozójának hogy biztosították a hátteret a nyugodt kísérleti munkához. Köszönettel tartozom Dario Quintavalle-nek és Nagy Kálmánnak a hasznos technikai tanácsokért. Korecz Lászlónak köszönöm, hogy mérési lehetőséget biztosított a Központi Kémiai Kutatóintézetben. Forró Lászlónak köszönöm a nyári gyakorlat lehetőségét Lausanne-ban. Náfrádi Bálintnak köszönhetem, hogy Lausanne-ban nem tettem semmit tönkre. Fehér Titusznak köszönöm, hogy bármikor fordultam hozzá elméleti kérdéssel, szívesen segített.

Acknowledgement

I am grateful to my parents for raising me. I thank my family for tolerating me. I thank Zsófi for her patience when I had to work. I am thankful to my supervisor Ferenc Simon for the professional help in physics and for weeding out mistakes in my English. I thank all workers of the Department of Experimental Physics for providing the conditions of successful research.

Contents

1 Introduction and overview

Needless to say that how promising material carbon nanotube is [1]. It has endless recent and future applications. It can be used as super-strong body armor which is lightweight and flexible. It is already a component of high-tech skis and new sport equipments with carbon nanotubes are on the horizon. A nanotube formed by joining nanotubes of two different diameters end to end can act as a diode, suggesting the possibility of constructing electronic computer circuits entirely out of nanotubes. Carbon nanotube diodes have photovoltaic effect [2], it can replace the crucial part of the solar cells, the indium tin oxide layer. Because of the extremely high curvature in the end of individual nanotubes, they can be used as electron gun and as cathode ray tubes in displays [3]. Based on the predicted high tensile strength of carbon nanotubes, it is a major candidate for being the building material of space elevator [4]. However, most of its applications need further research.

This degree work focuses on carbon nanotubes and fullerenes. The main topic is electron spin resonance (ESR) study of an interesting nanostructure: fullerenes encapsulated inside single-walled carbon nanotubes (SWCNTs), called peapods [5]. The interesting kind of peapods, which shows resonant absorption in ESR, is that with encapsulated magnetic fullerenes such as metallofullerenes with magnetic rare-earth ions [6] and the endohedral N@C_{60} [7] or C_{59}N [8]. From this large variety of structures, we worked with magnetic fullerene (every fullerene cage contains one atomic nitrogen) N@C_{60} encapsulated inside SWCNT. Thermal stability, hyperfine coupling and spin-lattice relaxation time is measured and compared with previous studies on the crystalline form of N@C_{60} . In crystalline form, N@C_{60} is sensitive to high temperature and annealing to $\sim$ 500 K was reported to irreversibly destroy the molecule by the escape of the nitrogen. This fact motivated us to study the temperature stability of N@C_{60} when it is encapsulated inside SWCNTs. The temperature dependence of the hyperfine coupling between the encapsulated nitrogen nuclear spin and its outer shell electrons depend on the possible vibrational modes of the nitrogen atom. We can obtain information about the possible distortion of the shape of the fullerene if it is encapsulated inside carbon nanotubes by measuring the temperature dependence of the hyperfine coupling. The modification to the electronic state of the molecule upon encapsulation is also of interest as it can provide information about the fullerene-tube interaction and about the electronic structure of the tubes themselves. Spin-lattice relaxation time is closely related to the electronic structure of SWCNTs. Most of the results of the present work has been published [9].

We show that the hyperfine splitting of the nitrogen in N@C$_{60}$, encapsulated inside SWCNT is temperature dependent. We can explain this with the interaction between the vibrational states of the nitrogen and the hyperfine splitting. The modelling of the excited vibrational states with a quantum harmonic oscillator gives a good fit to the experimental data. We show that N@C$_{60}$ encapsulated inside SWCNT is more stable at high temperature (620 K) than its pristine form, the crystalline N@C$_{60}$. With saturation ESR measurement we show that the T_1 relaxation time of N@C$_{60}$ is 10 times faster if it is encapsulated inside SWCNT than in crystalline form at room temperature. We suggest that the lowered symmetry and modified electronic structure of N@C$_{60}$ is responsible for this.

2 The experimental method

In this section we introduce the theoretical background needed to explain our experimental results.

2.1 Introduction

With ESR measurements, we can measure the ω frequency component of the magnetic spin susceptibility of an electronic system. For doing that, we need an external homogeneous magnetic field $\mathbf{B_0}$ parallel with the z axis and an electromagnetic field to measure the absorption and dispersion. In case of a free electron, the magnetic moment $\boldsymbol{\mu}$ is parallel with the spin $\boldsymbol{S}$, $\boldsymbol{\mu} = -g_e \mu_B \cdot \boldsymbol{S}$, where g_e is the electron spin g-factor and $\boldsymbol{\mu}$ and $\mathbf{S}$ are treated as vector operators, the spin is measured in $\hbar$ units, $\mu_B = 9.27 \cdot 10^{-24}$ J/T . In case of electron $S = 1/2$, the energy splitting is $\Delta E = \gamma_e \hbar B_0 = \hbar\omega_0$ where ω_0 is the resonance frequency of the absorbed or emitted photon, $\gamma_e = g_e \mu_B / \hbar$ is the gyromagnetic ratio of the electron ($\gamma_e / 2\pi$ =28GHz/T). For free electron, $g_e = 2.0023$, so if $\omega_0 = 2\pi \cdot 9$ GHz then the value of the magnetic field is $B_0 \approx 0.3$ T to fulfill the resonance condition. So we need a microwave (MW) source and detector to measure resonant absorption for this magnetic field.

2.2 Bloch equations

In the simplest case, we have one electron in the $\mathbf{B_0}$ magnetic field parallel with the z axis. The Hamilton operator which describes the system[10]:

$$\mathcal{H}_0 = \gamma_e \hbar \mathbf{S} \cdot \mathbf{B_0} = \gamma_e \hbar S_z B_0 \,. \tag{2.1}$$

If there is an operator $\mathcal{A}$, the time derivative of the expectation value is the well known formula:

$$\frac{d\langle \mathcal{A} \rangle}{dt} = \frac{i}{\hbar} \langle [\mathcal{H}_0, \mathcal{A}] \rangle \,. \tag{2.2}$$

Let's take the S operator, using the canonical commutation relations,

$$\left[S_i, S_j \right] = i \epsilon_{ijk} S_k \,, \tag{2.3}$$

where ϵ_{ijk} is the antisymmetric symbol and $i, j, k \in \{x, y, z\} \equiv \{1, 2, 3\}$. We can express the time derivative of the spin operator:

$$\begin{aligned}\frac{d\langle S_i\rangle}{dt} &= \frac{i}{\hbar}\langle[\gamma_e\hbar S_z B_0, S_i]\rangle = -\gamma_e B_0 \epsilon_{3ik}\langle S_k\rangle\ , \\ &= -\gamma_e \epsilon_{ik3}\langle S_k\rangle B_o = -\gamma_e\left[\langle \mathbf{S}\rangle \times \mathbf{B}_0\right]_i\ . \end{aligned} \tag{2.4}$$

Therefore, since $\mu = -\gamma_e\hbar\mathbf{S}$, we have the equation for the expectation value of magnetization,

$$\frac{d\langle\boldsymbol{\mu}\rangle}{dt} = -\gamma_e\langle\boldsymbol{\mu}\rangle \times \mathbf{B}_0\ , \tag{2.5}$$

which is just the classical equation. (2.5) holds true for a time-dependent magnetic field as well. If we solved (2.5) for a localized magnetic moment, we would get a periodic motion in time. The magnetic moment is precessing around the axis of the magnetic field with $\omega_0 = \gamma_e B_0$ Larmor (angular) frequency. Until now, we have not considered relaxation processes, without which the spin would precess forever. But there is always the environment, which can dissipate the potential energy of the magnetic moment. From now on we consider macroscopic number of spins or magnetic moments, thus instead of $\boldsymbol{\mu}$ we use $\mathbf{M}$, the magnetization vector of the sample, which is the expectation value of the total of the magnetic moment operators divided by the volume of the sample. We assume that the relaxation of M_z goes according to the equation

$$\frac{dM_z}{dt} = \frac{M_0 - M_z}{T_1}\ , \tag{2.6}$$

where M_0 is the thermal equilibrium magnetization, T_1 is the so called spin-lattice relaxation time. We assumed there is a static $\mathbf{B}_0$ magnetic field along the z axis, and a small rotating component $\mathbf{B}_1 = B_1\left(\mathbf{i}\cos(\omega t) + \mathbf{j}\sin(\omega t)\right)$. $\mathbf{B}$ is the sum of the two

$$\mathbf{B} = \mathbf{B}_0 + \mathbf{B}_1\ . \tag{2.7}$$

If we combine (2.6) with (2.5) we get

$$\frac{dM_z}{dt} = \frac{M_0 - M_z}{T_1} - \gamma_e\left[\mathbf{M} \times \mathbf{B}\right]_z\ . \tag{2.8}$$

The spin-lattice relaxation is an energy exchange between the spin system and the reservoir. There is an other process, which does not contribute to the energy change of the spin system, it accounts for the dephasing of individual magnetic moments. It is called spin-spin relaxation, the characteristic time is T_2 which most of the cases differs from T_1, the equation for

M_x and M_y will be similar for (2.8)

$$\frac{dM_x}{dt} = -\gamma_e \left[\mathbf{M} \times \mathbf{B}\right]_x - \frac{M_x}{T_2} \, ,$$
$$\frac{dM_y}{dt} = -\gamma_e \left[\mathbf{M} \times \mathbf{B}\right]_y - \frac{M_y}{T_2} \, . \tag{2.9}$$

A possible mechanism for T_2 in a solid is the dipolar interaction between like spins. (2.8) and (2.9) are called the Bloch equations [11]. To solve the Bloch-equations we use a coordinate system rotating about the z axis at an angular frequency ω which is the angular frequency of the irradiated microwave. The time derivative of any vector can be expressed in the rotating coordinate system

$$\frac{\delta \mathbf{F}}{\delta t} = \frac{d\mathbf{F}}{dt} - \mathbf{\Omega} \times \mathbf{F} \, , \tag{2.10}$$

where $d\mathbf{F}/dt$ is the time derivative in the laboratory coordinate system, $\mathbf{\Omega}$ is the angular velocity of the rotating system. We can eliminate the time dependence of $\mathbf{B}$ by setting $\mathbf{\Omega} = -\omega \mathbf{k}$, then $\mathbf{B}' = \mathbf{B}_0 + B_1 \mathbf{i}'$. The Bloch-equations read:

$$\frac{\delta M'_x}{\delta t} - \left[\mathbf{M}' \times \mathbf{\Omega}\right]_x = -\gamma_e \left[\mathbf{M}' \times \mathbf{B}\right]_x - \frac{M'_x}{T_2} \, ,$$
$$\frac{\delta M'_y}{\delta t} - \left[\mathbf{M}' \times \mathbf{\Omega}\right]_y = -\gamma_e \left[\mathbf{M}' \times \mathbf{B}\right]_y - \frac{M'_y}{T_2} \, ,$$
$$\frac{\delta M'_z}{\delta t} - \left[\mathbf{M}' \times \mathbf{\Omega}\right]_z = -\gamma_e \left[\mathbf{M}' \times \mathbf{B}\right]_z + \frac{M_0 - M'_z}{T_1} \, . \tag{2.11}$$

Neglecting the transient term, the steady state solution is:

$$M'_x = \omega_0 T_2 \chi_0 \frac{T_2}{1 + (\omega_0 - \omega)^2 T_2^2 + \gamma_e^2 B_1^2 T_1 T_2} B_1 \, ,$$
$$M'_y = \omega_0 T_2 \chi_0 \frac{(\omega_0 - \omega) T_2}{1 + (\omega_0 - \omega)^2 T_2^2 + \gamma_e^2 B_1^2 T_1 T_2} B_1 \, , \tag{2.12}$$

where $\omega_0 = \gamma_e B_0$ is the Larmor frequency, $\chi_0 = \mu_0 \frac{M_0}{B_0}$ the Curie susceptibility, μ_0 is the vacuum permeability. In the laboratory coordinate system M_x is related to M'_x and M'_y

$$M_x = M'_x \cos(\omega t) + M'_y \sin(\omega t) \, . \tag{2.13}$$

If we write the magnetic field as being linearly polarized,

$$B_x = 2B_{x0}\cos(\omega t)\,, \tag{2.14}$$

then we see that M_x is proportional to B_{x0} and we can write

$$M_x = \frac{1}{\mu_0}(\chi' \sin(\omega t) + \chi'' \cos(\omega t))B_{x0}\,, \tag{2.15}$$

defining the quantities χ' and χ''. By using (2.12) and (2.15), we get

$$\begin{aligned} \chi'(\omega) &= \chi_0 \frac{\omega_0(\omega_0-\omega)T_2^2}{1+(\omega_0-\omega)^2T_2^2+\gamma_e^2B_1^2T_1T_2}\,, \\ \chi''(\omega) &= \chi_0 \frac{\omega_0 T_2}{1+(\omega_0-\omega)^2T_2^2+\gamma_e^2B_1^2T_1T_2}\,. \end{aligned} \tag{2.16}$$

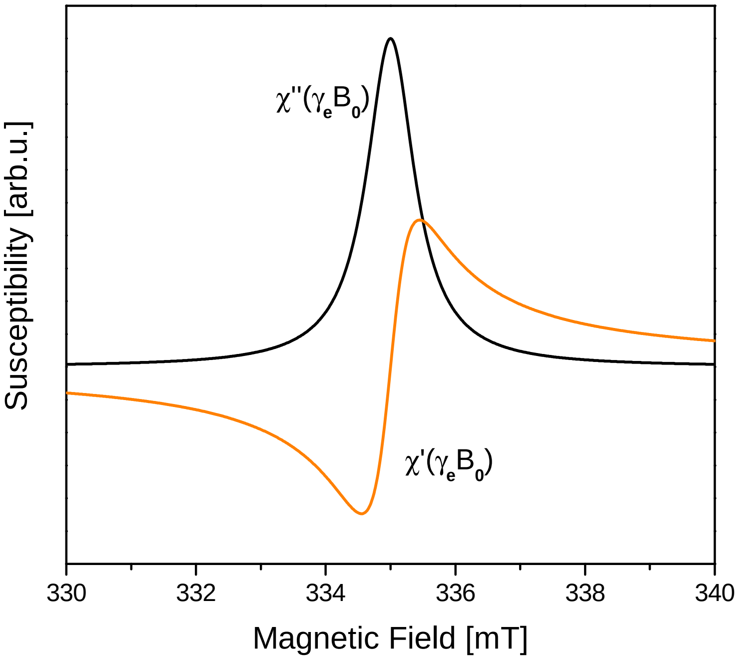

Fig. 2.1: The real and imaginary part of the susceptibility. Instead of ω, $\omega_0 = \gamma_e B_0$ is varied. The HWHM of $\chi''(\omega)$ is proportional to $1/T_2$ in the non saturating limit.

χ' is related to the dispersion of the microwave, χ'' is related to the absorption of the microwave. The usual way to measure ESR spectra is to scan the B_0 magnetic field, while ω is constant, the measured quantity is χ''.

If we plot χ'' against ω_0 (see Fig. 2.1) the function is called Lorentzian. We can introduce the saturation factor $s = 1/(1+\gamma_e^2 B_1^2 T_1 T_2)$. The term $\gamma_e^2 B_1^2 T_1 T_2$ is proportional to the microwave power P. If P is small then $s \simeq 1$, it is called the non saturating limit (NSL). In this case, the solutions to the Bloch-equation reduce to

$$\begin{aligned} \chi'(\omega)_{NSL} &= \chi_0 \frac{\omega_0(\omega_0-\omega)T_2^2}{1+(\omega_0-\omega)^2 T_2^2}\,, \\ \chi''(\omega)_{NSL} &= \chi_0 \frac{\omega_0 T_2}{1+(\omega_0-\omega)^2 T_2^2}\,. \end{aligned} \tag{2.17}$$

In the non saturating limit both part of the susceptibility is constant against P and the half width half maximum (HWHM) of the signal (we denote it as ΔB) is

$$\Delta B = \frac{1}{\gamma_e T_2}\,. \tag{2.18}$$

If the MW power is increased above the NSL, χ'' will be reduced. It is called saturation.

It is useful to introduce the complex susceptibility $\chi = \chi' - i\chi''$ and writing $B_x^C(t) = B_{x0}e^{i\omega t}$ then

$$M_x^C(t) = \frac{1}{\mu_0}\chi \cdot B_x^C(t)\,, \tag{2.19}$$

where the ^{C} means complex number. To calculate the power absorbed by the sample, we use results from linear response theory [12]. The Hamiltonian of the system is

$$\mathcal{H} = \mathcal{H}_0 + \mathcal{H}_1 = -M_z B_0 - \mathbf{M}\cdot\mathbf{B}_1, \tag{2.20}$$

assuming that $B_1 \ll B_0$, the second term can be treated as perturbation. The time dependent energy of the system

$$E(t) = \langle\psi|\mathcal{H}_1|\psi\rangle\,, \tag{2.21}$$

where ψ is the time independent eigenfunction of $\mathcal{H}_0$. By definition the absorbed power is

$$P(t) = \frac{dE(t)}{dt} = \langle\psi|\frac{d}{dt}(-\mathbf{M}\cdot\mathbf{B}_1(t))|\psi\rangle = -\langle\mathbf{M}\rangle\frac{d\mathbf{B}_1(t)}{dt}\,. \tag{2.22}$$

Taking the Fourier transform of both terms, we get

$$\begin{aligned} \frac{d\mathbf{B}_1(t)}{dt} &= \frac{1}{\sqrt{2\pi}}\int_{-\infty}^{\infty} d\omega'\mathbf{B}_1(\omega')e^{i\omega' t}\,, \\ \langle\mathbf{M}\rangle &= \int_{-\infty}^{\infty} d\omega'\chi(\omega')\mathbf{B}_1(\omega')e^{i\omega' t}\,, \end{aligned} \tag{2.23}$$

where $\chi(\omega')$ is the complex susceptibility. Assuming the perturbative magnetic field is a cosine function of time, $\mathbf{B}_1(t) = \Re(\mathbf{B_1}e^{i\omega t}) = \mathbf{B_1}\left(e^{i\omega t} + e^{-i\omega t}\right)$, the Fourier transform is

$$\mathbf{B_1}(\omega') = \frac{1}{\sqrt{2\pi}}\mathbf{B_1}\left[\delta(\omega' - \omega) + \delta(\omega' + \omega)\right] \ . \tag{2.24}$$

Using (2.23) and (2.24) we get

$$P = -\frac{i}{2\pi}|\mathbf{B_1}|^2\omega\left[\chi(-\omega) - \chi(\omega)\right] \ . \tag{2.25}$$

Since the response to a real function has to be real as well, χ has to fulfill $\chi(-\omega') = \chi(\omega')^*$ equation. The final form of the absorbed power is

$$P = -\frac{i}{2\pi}|\mathbf{B_1}|^2\omega\Im[\chi^*(\omega) - \chi(\omega)] = \frac{1}{\pi}|\mathbf{B_1}|^2\omega\chi''(\omega) \, . \tag{2.26}$$

2.3 Saturation

In most of the case we try to avoid the saturation of the ESR signal, but to measure the relaxation times with cwESR the only possibility is to successively saturate the ESR signal and measure the integrated intensity of the absorption signal. The integrated intensity of the signal from (2.16) is [13]

$$I = \int_{-\infty}^{\infty}\chi'' dB_0 = M_0\pi\frac{1}{\sqrt{1 + \gamma_e^2 B_1^2 T_1 T_2}} \ . \tag{2.27}$$

Clearly the integrated intensity drops with the square root of the saturation factor whereas the signal peak amplitude drops with s. This is due to the fact, that saturation is less effective off-resonance, therefore the total line intensity saturates slower with s than expected from the peak height. The integrated susceptibility will reduce if the microwave power is increased since B_1^2 is proportional to the microwave power, the linewidth will change as well

$$\Delta B' = \Delta B\sqrt{1 + \gamma_e^2 B_1^2 T_1 T_2} \, , \tag{2.28}$$

where ΔB is the HWHM value of the Lorentzian, we can define $T_2' = 1/(\gamma_e \Delta B')$. We can see, that increasing power increases the linewidth. If we measure the total intensity of the signal against the microwave power we can determine $T_1 \cdot T_2$ by fitting the obtained curve with (2.27).

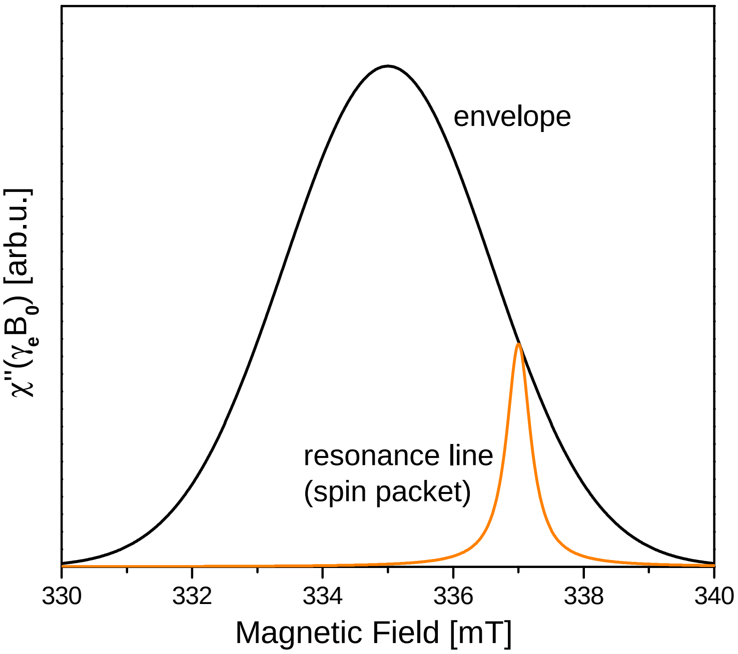

Fig. 2.2: Absorption envelope and one of its individual resonant lines (spin packets).

Following Portis [14] it was recognized that saturation induced broadening is not necessarily observed. In solids, the observed HWHM linewidth is $\Delta B^* = 1/(\gamma_e T_2^*)$ which is much larger than the $\Delta B = 1/(\gamma_e T_2)$ due to static inhomogeneities of the local magnetic field. This can result from defects, inhomogeneities of B_0, hyperfine interaction, etc. $1/(\gamma_e T_2)$ related to spin-spin interaction is called the width of a spin packet. This situation is shown on Fig. 2.2.

There is a possible method to measure T_2 with cwESR. One can measure the HWHM value of the non saturated Lorentzian shaped signal (as we will see later the measured signal is the derivative of the Lorentzian due to the detection method, but with numerical integration the absorption lineshape can be produced) which according to the Bloch-equations (2.16) equals to $1/(\gamma T_2)$. But this has to be used carefully because of the inhomogeneous broadening of the line, the FWHM of inhomogeneously broadened lines gives T^* which always smaller or equal to T_2

$$\frac{1}{T^*} = \frac{1}{T_2} + \frac{1}{T_{ih}}, \tag{2.29}$$

where $1/T_{ih}$ is the inhomogeneous broadening.

2.4 Static spin susceptibility

In materials where there is no interaction between the localized spins, the magnetic state is called paramagnetism. Thus in paramagnetic materials, every extensive physical quantity scales with the number of moments in the material. So we can make our calculation for individual magnetic moment. We label the angular momentum states of an atom as $|J, J_m\rangle$, where $J = L + S$ is the total angular momentum, J_m is the value along the quantization axis. The z component of the magnetic moment of an atom with electron spin and orbital magnetic moment is

$$\mu_z(J_m) = -g_J \mu_B J_m \,, \tag{2.30}$$

where g_J is the Landé g-factor [10]

$$g_J = 1 + \frac{J(J+1) + S(S+1) - L(L+1)}{2J(J+1)} \,. \tag{2.31}$$

In the static B_0 magnetic field, the energy of the electron is $E_m = g_J \mu_B m B_0$. In a canonical ensemble, the probability of the states

$$P_m = \frac{e^{-\beta E_m}}{\sum e^{-\beta E_m}} \,, \tag{2.32}$$

where $\beta = 1/(k_B T)$, T is the lattice temperature. The expectation value of the magnetic moment is

$$\langle \mu_z \rangle = \sum_m \mu_z(m) \cdot P_m = \frac{\sum\limits_{m=-J}^{J} g_J \mu_B m \exp(-\beta g_J \mu_B m B_0)}{\sum\limits_{m=-J}^{J} \exp(-\beta g_J \mu_B m B_0)} \,. \tag{2.33}$$

The partition function of the canonical ensemble is

$$Z = \sum_{m=-J}^{J} \exp(-\beta g_J \mu_B m B_0) \,, \tag{2.34}$$

the summa is a geometric series. Using (2.34) we get

$$\langle \mu_z \rangle = \frac{1}{B_0} \frac{\partial}{\partial \beta} \ln Z \,. \tag{2.35}$$

After straightforward calculation, taking into account that we have n paramagnetic atoms in a volume V we obtain

$$M_0 = \frac{n g_J \mu_B J}{V} B_J(x) \, , \tag{2.36}$$

where $x = g_J \mu_B J B_0 \beta$ and $B_J(x)$ is the Brillouin function which reads

$$B_J(x) = \frac{2J+1}{2J} \coth\left(\frac{2J+1}{2J} x\right) - \frac{1}{2J} \coth\left(\frac{1}{2J} x\right) \, . \tag{2.37}$$

If B_0 is large enough M_0 saturates, if B_0 is small or the temperature is high enough, M_0 is proportional to the magnetic field, using

$$M_0 = \frac{1}{\mu_0} \chi_0 B_0 \, , \tag{2.38}$$

where χ_0 is the static susceptibility, one gets

$$\chi_0 = \mu_0 \lim_{B_0 \to 0} \frac{M_0}{B_0} = \mu_0 g_J^2 \frac{J(J+1)\mu_B^2}{3 k_B T} \frac{n}{V} \, , \tag{2.39}$$

this is the Curie susceptibility. If the atom has spin of 1/2 and no orbital moment then

$$\chi_0 = \mu_0 \frac{g_e^2 \mu_B^2}{4 V_c k_B T} \simeq \mu_0 \frac{\mu_B^2}{V_c k_B T} \, , \tag{2.40}$$

where $V_c = V/n$ is the density of magnetic moments.

2.5 Hyperfine splitting

Since the source of an ESR spectrum is a change in an electron's spin state, it might be thought that all ESR spectra would consists of a single line. However, the interaction of an unpaired electron, by way of its magnetic moment, with nearby nuclear spins, results in additional allowed energy states and, in turn, multi-lined spectra. In such cases, the splitting between the ESR spectral lines indicates the degree of interaction between the unpaired electron and the perturbing nuclei. The hyperfine coupling constant of a nucleus is directly related to the spectral line spacing and, in the simplest cases, is essentially the spacing itself. Two common mechanisms by which electrons and nuclei interact are Fermi-contact interaction and dipolar interaction.

The magnetic field of a nuclear magnetic moment being at the origin of the coordinate system is

$$\mathbf{B}_{nuc}(\mathbf{r}) = \frac{\mu_0}{4\pi r^3}\left(3(\mathbf{m}\cdot\hat{\mathbf{r}})\hat{\mathbf{r}} - \mathbf{m}\right) + \frac{2\mu_0}{3}\mathbf{m}\delta^3(\mathbf{r})\,, \tag{2.41}$$

where $\mathbf{r}$ is the vector from the position of the nucleus to the position where the field is being measured, $\hat{\mathbf{r}} = \mathbf{r}/r$ is the unit vector parallel to $\mathbf{r}$, $\mathbf{m}$ is the dipole moment of the nucleus. The first term accounts for the dipolar interaction, the second for the Fermi-contact interaction. The perturbing Hamiltonian is

$$\mathcal{H}_{hyp} = -\gamma_e \hbar \mathbf{S} \int |\psi(\mathbf{r})|^2 B_{nuc}(\mathbf{r}) d^3\mathbf{r}\,, \tag{2.42}$$

where $|\psi(\mathbf{r})|^2 d^3\mathbf{r}$ is the probability of finding the electron in the volume $d^3\mathbf{r}$. If the electron's wave function has spherical symmetry, the dipolar interaction is cancelled out, only the Fermi-contact interaction will be non-zero. In this case, the simplified perturbing Hamiltonian is the following

$$\mathcal{H}_{hyp} = -\frac{2\mu_0}{3}|\psi(0)|^2 \gamma_e \hbar \mathbf{S}\cdot\mathbf{m}\,. \tag{2.43}$$

The magnetic moment of a nucleus can be written in the form of $\mathbf{m} = \gamma_{nuc}\hbar\mathbf{I}$, where γ_{nuc} is the gyromagnetic ratio of the nucleus, $\mathbf{I}$ is the spin operator of the nucleus. We can define the scalar A through

$$A = -\frac{2\mu_0}{3}\gamma_e \hbar \gamma_{nuc} \hbar |\psi(0)|^2\,. \tag{2.44}$$

In the general case, when the dipolar interaction is not cancelled out, A is a 3x3 tensor with 2 indexes: A_{ij}. The general formula for the hyperfine interaction is

$$\mathcal{H}_{hyp} = \sum_{\{i,j\}=1}^{3} S_i A_{ij} I_j\,. \tag{2.45}$$

The above can be demonstrated with the spectra of Mn:MgO. It consists six equidistant lines see Fig. 2.3. The spectra shows the resonant absorption of d shell electrons of the manganese. The reason of the 6 lines is that the nucleus of ^{55}Mn, which has nuclear spin of $I = 5/2$, in the B_0 static external magnetic field can possess 6 different values of magnetic moment along the z axis. Since at room temperature the $k_B T$ energy is much bigger than the nuclear Zeeman energy at conventional field strengths, every level has a same population which is constant during the characteristic time of an

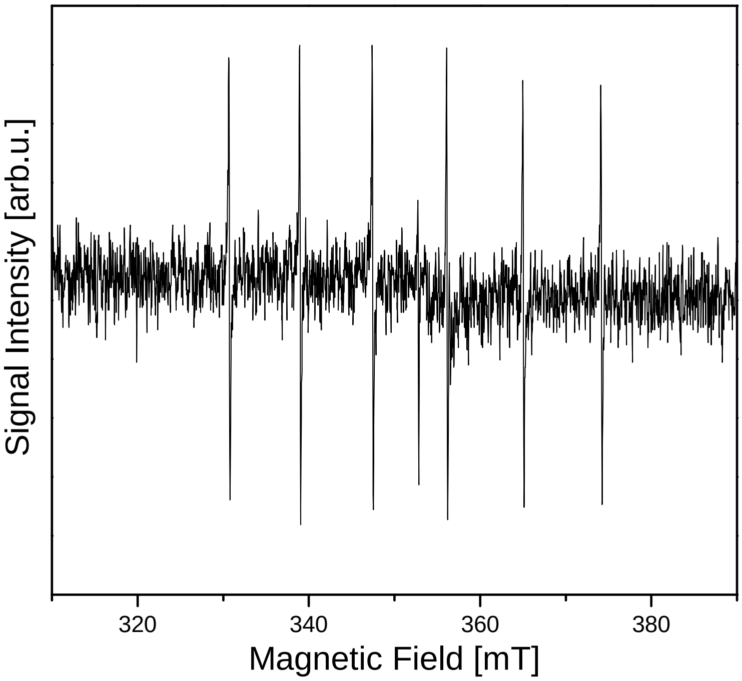

Fig. 2.3: ESR spectra of Mn:MgO, the concentration of Mn is 1.5 ppm, the single line around g =2 (B = 353 mT) is due to the presence of impurities.

ESR measurement. Thus electrons of Mn feel a locally modified magnetic field that gives the 6 equidistant lines, this is the hyperfine splitting. In case of Mn the hyperfine coupling is isotropic, thus the perturbing Hamiltonian is

$$\mathcal{H}_{hyp} = A_{iso}\mathbf{S} \cdot \mathbf{I} \,. \tag{2.46}$$

Our wave functions are product of the electronic spin state and nuclear spin state, in the simplest case with one electron around a nucleus

$$|\psi\rangle = |S, m_S\rangle |I, m_I\rangle \,. \tag{2.47}$$

If the magnetic field is parallel with the z axis, the expectation value of nuclear angular moment in the x-y plane is zero, $\langle I_x \rangle = \langle I_y \rangle = 0$ so the Hamiltonian of the system is

$$\mathcal{H} = \mathcal{H}_0 + \mathcal{H}_{hyp} = -\gamma_e \hbar \left(B_0 - \frac{A m_I}{\gamma_e \hbar} \right) S_z \,, \tag{2.48}$$

where m_I is the eigenvalue of I_z, every possible value is equally probable. Clearly, the resonance field is shifted, it can have 6 different values

$$B_{res} = B_0 - \frac{A m_I}{\gamma_e \hbar} \,, \tag{2.49}$$

that explains the 6 resonance lines.

2.6 Spectrometer

Fig. 2.4: Bruker Elexsys E500 spectrometer

For most of our measurements we used a Bruker Elexsys E500 cwESR spectrometer (see Fig. 2.4), found in the laboratory of Korecz László[1]. From the previous section we see, that a microwave cavity, a microwave source, a detector and homogeneous magnetic field is required for the ESR measurements. To control the phase and intensity of the microwave properly and to increase the signal to noise ratio a conventional cwESR spectrometer consists of additional devices. Fig. 2.5 shows the schematic diagram. This spectrometer runs on X band, that means the frequency of the microwave is about 9 GHz, the maximum power of the MW source is 100 mW. Since the MW detector has a non zero working point, it requires a MW bias, thus the microwave is split into two paths. One goes through attenuator 1 to adjust the operating point of the detector, this is called the reference arm. The other goes through attenuator 2 to select the incident power to the sample. The circulator guides the microwave from the source to the cavity and from the

---

[1] Chemical Research Center, Hungarian Academy of Sciences

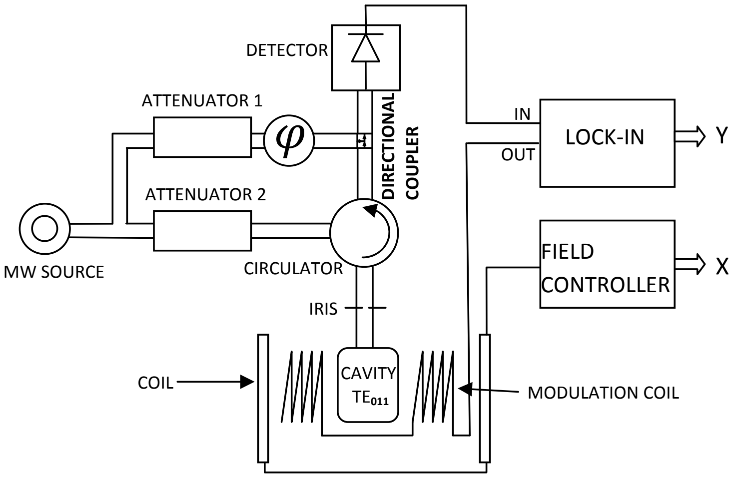

Fig. 2.5: Schematic diagram of cwESR spectrometer. X is the B_0 magnetic field strength, Y is the measured voltage by the lock-in detector. A computer is used for recording, storing and analyzing spectra.

cavity to the detector, any other way is forbidden. In the detector, the two microwaves are added and by adjusting the φ phase shifter, constructive interference is established. The iris can control the reflectance of the cavity by changing the diameter of the waveguide at a certain point. The detector will be most sensitive if the reflectance of the cavity is zero, in this case when resonant absorption occurs, a small change in χ'' makes a big difference of MW intensity at the detector. The spectra is the measured voltage by the lock-in detector (Y) against the B_0 magnetic field (X). Although it would be reasonable, the measured signal is not proportional to the absorbed microwave power by the sample. The measured signal is proportional to the square root of the microwave radiation power of the $\mathbf{M}$ induced magnetic moment. Let the electric field of the reference microwave on the surface of the detector be

$$E_0 \exp(i\omega t + i\varphi) \, , \tag{2.50}$$

where E_0 is the scalar amplitude (we disregard polarization), ω is the frequency of the microwave, φ is the phase shift. The electric field of the induced magnetic moment on the surface of the detector is

$$dE \exp(i\omega t + i\varphi_0) = CM \exp(i\omega t + i\varphi_0) = CB_1(\chi' - i\chi'') \exp(i\omega t + i\varphi_0) \, , \tag{2.51}$$

where C is constant, φ_0 is a constant phase shift because of time of travel difference, B_1 is the magnetic field of the microwave at the sample. This electric field induces a current at the detector, the RMS value of the current is proportional to

$$I_{RMS}^2 \propto |E_0 \exp(i\omega t + i\varphi) + dE \exp(i\omega t + i\varphi_0)|^2 \; . \tag{2.52}$$

Assuming $dE \ll E_0$ the $O(dE^2)$ is negligible, the result

$$I_{RMS}^2 = I_{OP}^2 + CE_0 B_1 \chi' \cos(\varphi - \varphi_0) + CE_0 B_1 \chi'' \sin(\varphi - \varphi_0) \; . \tag{2.53}$$

The measured signal is proportional to I_{RMS}^2, thus we can measure the dispersion signal if we set $\varphi = \varphi_0$ or the absorption signal if we set $\varphi = \varphi_0 + 90°$. In the following part we always set $\varphi = \varphi_0 + 90°$ and CE_0 is constant thus the measured signal is

$$I \propto B_1 \chi'' \; . \tag{2.54}$$

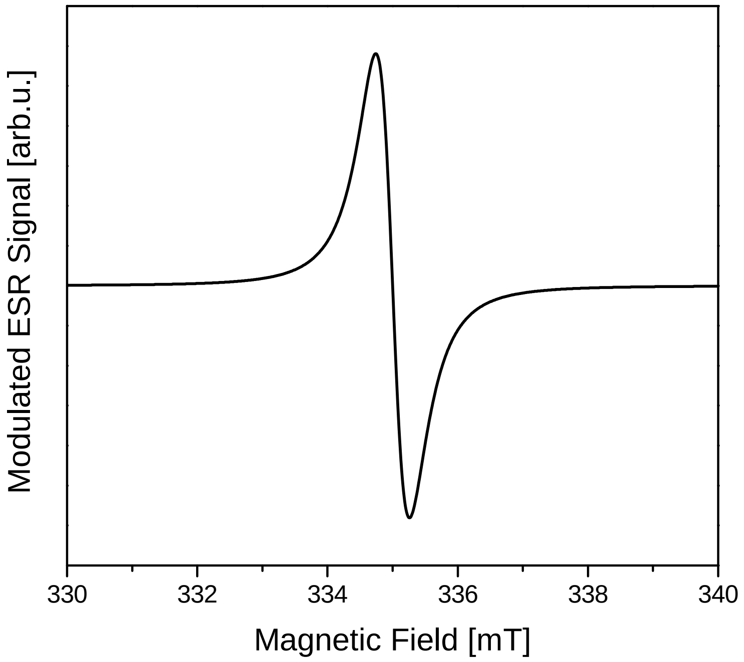

Fig. 2.6: The ESR spectra of a single absorption line. The measured signal is the first derivative of $\chi''(\gamma_e B_0)$. The peak to peak distance is proportional to $1/T_2$ in the non saturating limit.

The magnetic field is generated by resistive coils, which are driven by a current generator directly controlled by a computer. The signal of the detector is not directly recorded and to increase the signal to noise ratio a lock-in amplifier is introduced. The cavity has two small modulation coils which are driven by the lock-in and the in-phase component of the signal of the detector is recorded by a PC. The modulation frequency is 100 kHz, higher value is limited by the inductance of the modulation coils. The integration time is 30 ms which means ≈30 Hz bandwidth. It is a compromise between signal to noise ratio and measurement time. For small B_{mod} modulation amplitude the measured signal is essentially the first derivative of the line shape see Fig. 2.6, and the measured signal is proportional to the modulation amplitude

$$I \propto B_1 \frac{d\chi''}{dB_0} B_{mod} \,. \tag{2.55}$$

In the following, we always normalize the spectra with the modulation amplitude.

2.7 Microwave cavity

The knowledge of the microwave power in the place of the sample is important for the saturation ESR experiments, which are discussed below. The Bruker Elexsys E500 spectrometer employs a cylindrical cavity, which supports the TE_{011} mode, where the subscripts 0,1,1 refer to the number of half cycle variations of standing waves in the angular (ϕ), radial (r) and longitudinal (z) directions respectively, see Fig. 2.7. The special construction of the cavity provides that other modes have negligible amplitude. The sample is located in the center of the resonant cavity, the magnetic field

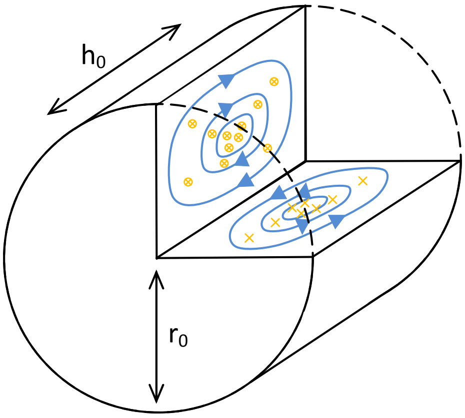

Fig. 2.7: Electromagnetic field of TE_{011} mode in cylindrical cavity, blue is magnetic field, orange is electric field. r_0 is the radius, h_0 is the length of the cavity.

has an antinode there. Let the cavity radius be r_0 and the length be h_0. To analyze saturation curves, we need to know the exact magnitude of magnetic field in the location of the sample. In this section we calculate the perturbative magnetic field induced by the microwave, the static B_0 magnetic field is omitted. The volume averaged magnetic field of the TE_{011} mode [13]

$$\langle B_1^2 \rangle_C = 0.0811 B_{cav}^2 \,, \tag{2.56}$$

where $\langle\rangle_C$ is the volume average in the cavity, B_{cav} is the maximum amplitude of the microwave magnetic field in the cavity. If a small sample is located exactly in the center of the resonant cavity, one gets [13]

$$\langle B_1^2 \rangle_S = \frac{B_{cav}^2}{1 + (0.82 r_0/h_0)^2} \,, \tag{2.57}$$

where $\langle\rangle_S$ is the average value of magnetic field at the sample. The amplitude of the magnetic field in the cavity is proportional to the incident microwave power. To determine the proportionality, the Q, quality factor has to be introduced. Q-factor is by definition

$$Q = 2\pi \frac{\text{energy stored}}{\text{energy dissipated per cycle}} \,. \tag{2.58}$$

In case of electromagnetic wave, the energy stored in the cavity is [15]

$$E_{MW} = \int_{cavity} w dV = \int_{cavity} \frac{1}{2} \left(\epsilon_0 \overline{\mathbf{E}^2} + \frac{1}{\mu_0} \overline{\mathbf{B}^2} \right) dV = \int_{cavity} \frac{1}{\mu_0} \overline{\mathbf{B}^2} dV \,, \tag{2.59}$$

where the bar sign means time average. Using (2.59) one gets

$$Q = 2\pi \frac{\frac{1}{2\mu_0} \langle B_1^2 \rangle_C \cdot V_C}{P \cdot T} \,, \tag{2.60}$$

where V_C is the volume of the cavity, T is the period of microwave, 1/2 is used instead of time average. Finally putting all these together, the magnetic field in the sample (assuming the relative permeability of the sample is close to one)

$$\langle B_1^2 \rangle_S = \frac{2\mu_0 P Q}{\omega V_C} \frac{1}{0.0811 \cdot (1 + (0.82 r_0/h_0)^2)} \,. \tag{2.61}$$

To make an ESR transition, only the circularly polarized wave is effective, which rotates in the right direction. The linearly polarized wave can be decomposed to 2 circularly polarized waves which rotate in the opposite directions, the amplitude of one rotating component is half of the linearly polarized wave

$$\langle B_1^2\rangle_S^{ROT} = \frac{1}{4}\cdot\frac{2\mu_0 PQ}{\omega V_C}\frac{1}{0.0811\cdot(1+(0.82r_0/h_0)^2)}\,. \tag{2.62}$$

From here on B_1 refers to $\langle B_1^2\rangle_S^{ROT}$. The size of the cavity of Bruker spectrometer is $r_0 = 20.48$ mm and $h_0 = 2\cdot r_0 = 40.97$ mm, the angular frequency of the microwave is $\omega = 2\pi\cdot 9$ GHz, with these values (2.62) will be

$$\langle B_1^2\rangle_S^{ROT} = 2.17\cdot 10^{-12}\left[\mathrm{T}^2/\mathrm{W}\right]\cdot PQ\,. \tag{2.63}$$

3 Materials

In this section we introduce the relevant physical properties of fullerenes and nanotubes and its derivatives. We explain the synthesis of N@C_{60}@SWCNT as well.

3.1 Fullerene and its derivatives

The C_{60} molecule was discovered in 1985 by Kroto *et al.* [16]. A fullerene molecule contains 60 carbon atoms in a football shaped structure. The 60 carbon atoms in C_{60} are known to be located at the vertices of a truncated icosahedron where all carbon sites are equivalent. Each carbon atom is trigonally bonded to three other carbon atoms in an sp^2-derived configuration. The truncated icosahedron has 20 hexagonal faces and 12 pentagonal faces. Two single C-C bonds are located along a pentagonal edge at the fusion of a hexagon and a pentagon, the bond length is 1.455 Å. The double bonds are located at the fusion between two hexagons, the length is 1.391 Å. In the solid state, the C_{60} crystallize into an fcc cubic structure with a lattice constant of 1.417 nm, the van der Waals diameter is about 1 nm.

N@C_{60} is a fullerene that contains one nitrogen atom inside the C_{60} cage which is also called endohedral position [17]. It can be produced by the nitrogen implantation method but to gain measurable amount of N@C_{60} , additional purification is needed with high performance liquid chromatography.

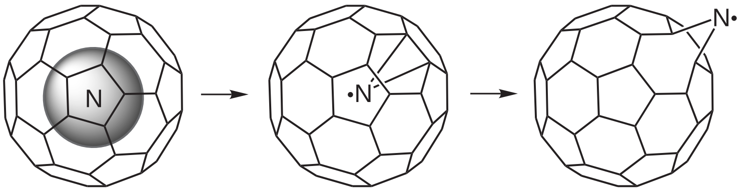

Fig. 3.1: Escape mechanism of nitrogen from N@C_{60} [18]. It breaks a double bond of two carbon atom and swings to the outside

The N atom is in its atomic state with the electron spin in the $S = 3/2$ configuration due to the Hund's rules. The electronic wave function is compressed [19] due to the interaction with the cage. Above 510 K, the structure is unstable [20] but the temperature of decomposition is smoothed. The calculations show [18] that the energy of the nitrogen rises continuously with the displacement from the center of the cage. Coming closer to the cage, the nitrogen forms an endohedral complex with two carbon atoms and reaches a local minimum for the doublet ($S = 1/2$) configuration. In the last step, the nitrogen atom swings through the bridge to the outside (see Fig. 3.1).

Fullerenes are soluble in many solvents. Common solvents for the fullerenes include aromatics, such as toluene, and others like carbon disulfide. Solutions of pure Buckminsterfullerene have a deep purple color. We used toluene ($C_6H_5CH_3$) mostly as a solvent in the encapsulation studies, in which the approximate saturated concentration of C_{60} is 3 mg/ml [21].

Our sample contains N@C_{60} of 400 ppm concentration with C_{60}, N@C_{60}:C_{60} refers to the crystallized form of this mixture. To measure it with ESR, we carefully degassed the sample and sealed it in quartz tube under He atmosphere. In the following we refer to this sample as "crystalline".

3.2 Nanotubes

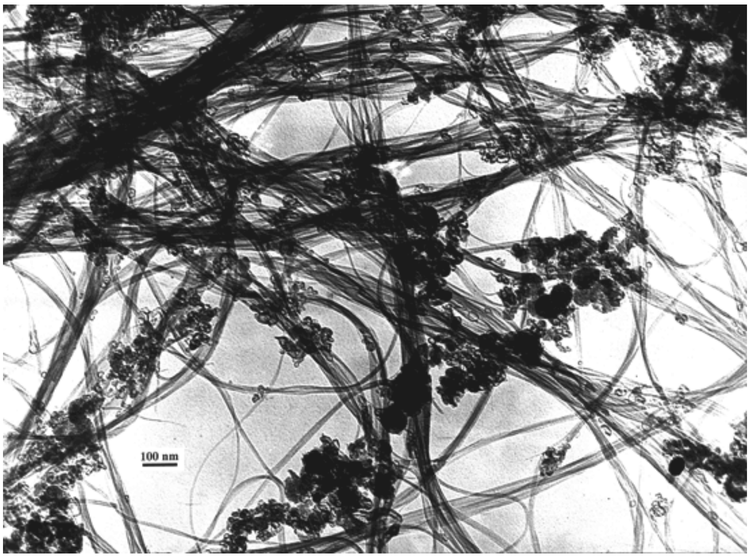

Fig. 3.2: Transmission electron microscope (TEM) image of SWCNT from Nanocarblab [22].

The first scientific article about carbon nanotubes was published in 1991 [23] by Iijima, it reports the discovery of multi-walled carbon nanotubes (MWCNT). Two years later single-walled nanotubes were discovered by Iijima and Ichihashi [1]. The structure of a SWCNT can be represented by wrapping a one-atom-thick layer of graphite called graphene into a seamless cylinder [24]. The way the graphene sheet is wrapped is represented by a pair of indices (n, m) called the chiral vector. The integers n and m denote the number of unit vectors along two directions in the honeycomb crystal lattice of graphene. If $m = 0$, the nanotubes are called "zigzag". If $n = m$, the nanotubes are called "armchair". Otherwise, they are called "chiral". Single-walled nanotubes exhibit promising electric properties that are not shared by the multi-walled carbon nanotube (MWCNT) variants. SWCNTs can be metallic if $2n + m = 3q$ where q is an integer, otherwise they are semiconducting. Since the production of SWCNTs is not chirality specific, every sample contains metallic (33 m/m%) and semiconducting nanotubes as well. Without functionalization, nanotubes are not soluble in common solvents like toluene, they just form a suspension after a few minutes of sonication.

We used commercial purified SWCNTs (Nanocarblab, Moscow, Russia, purity 50 m/m%) as a black powder, wich contains nanotube bundles, the diameter of the tubes has Gaussian distribution with expectation value of 1.4 nm and variance of 0.1 nm. It is produced by the Arc-discharge method using Y:Ni catalyst [25]. In the bundles tubes are parallel oriented in a hexagonal lattice. They are kept together by van der Waals forces (see Fig. 3.2).

3.3 Peapods

Peapod is a SWCNT filled with fullerene molecules [5]. Fullerenes forms a one dimensional lattice inside the SWCNT with the average fullerene-fullerene distance of 0.97 nm [27]. For the fullerenes it is energetically favorable being inside the tube but there is a non-zero activation energy needed to form the peapod structure [28]. There are different methods to provide the required energy. At high temperature (650 °C) the vapor pressure is the driving force of peapod formation but this process has a drawback, $N@C_{60}$ would decompose at such high temperature. We used a different method, a suspension of SWCNT in toluene containing dissolved $N@C_{60}:C_{60}$ was sonicated for 2 hours, filtered with a 0.4 μm pore size filter and dried at room temperature to obtain samples in the form of bucky-paper. Raman studies indicate that significant filling factor can be achieved [7], on TEM pictures the peapod structure is clearly visible (see Fig. 3.3).

For ESR measurements, we ground the bucky-paper to avoid skin effect of the exciting microwaves since the bucky paper is a good conductor

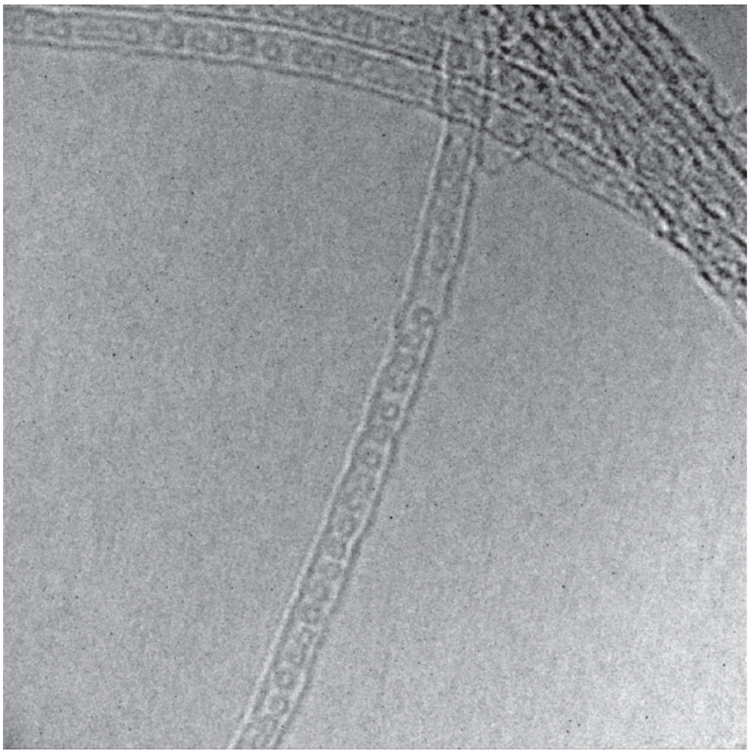

Fig. 3.3: TEM image of a SWCNT filled with C_{60} , the structure is called peapod (image from Ref. [26])

itself and absorbs the microwave. After carefully degassing the powder, we sealed it in quartz tube under He atmosphere, in the following we refer to this sample as ″peapod″.

4 Results and discussion

Here we present the new results achieved in this work.

4.1 Measuring the Concentration of N@C$_{60}$ in the peapod material

The concentration of N@C$_{60}$ is an important parameter as it is a measure of the filling efficiency. To determine the concentration of N@C$_{60}$ in peapod material, we compared the susceptibility with other paramagnetic samples. We also checked whether the signal intensity depends on the position of the sample in the cavity, but within ±5% error it is independent of the position. We used as reference CuSO$_4$.5H$_2$O and Mn:MgO where the concentration of Mn is 1.5 ppm. Each sample has Curie-susceptibility at room temperature, but the $S(S+1)$ prefactor is different, CuSO$_4$ has $S = 1/2$ spin, while Mn has $S = 5/2$ spin, and because of zero field splitting only the $|-1/2\rangle \rightleftharpoons |1/2\rangle$ transitions are visible. We have to calculate the $\langle s, m-1|S_-|s, m\rangle$ matrix elements and get the probability of the allowed transition. Thus we get $''S(S+1)'' = 9/4$ for Mn. The ESR intensity of the signal (non saturated, non overmodulated) is

$$I \sim \chi_0 \cdot \sqrt{P} \cdot N_{spins} \cdot B_{mod} \,, \tag{4.1}$$

which is (2.27) if the saturation factor $s = 1$, $\sqrt{P}$ comes from (2.54) and B_{mod} from (2.55). For the 2 reference samples we know the number of spins and measured signal intensity, thus we can calculate the accuracy of our measurements by comparing the two intensities. The error of the measured absolute number of spins is ±20%. If the SWCNTs are fully packed with fullerenes we have 15 m/m% fullerenes in the sample (50 m/m% of the sample is carbon impurities, and the mass of the tubes are twice as the mass of the fullerene per length). In case of N@C$_{60}$ the $S(S+1)$ expression in Curie-susceptibility is 15/4, because atomic nitrogen is in quartet state. If we regard this as 100% efficient filling, from the measurement of paramagnetic susceptibility we get 2% filling efficiency. This is a lower estimate because of MW shielding effects, inside nanotube bundles the microwave can be shielded thus the ESR signal of the spins deep inside the bundles can be suppressed.

In [7] they used the same filling method and a somewhat higher 5±0.5% filling efficiency was reported.

	Mn:MgO	$CuSO_4.5H_2O$	N@C_{60}@SWCNT
$''S(S+1)''$	9/4	3/4	15/4
$''M_{mol}$ [g/mol]$''$	40	249.5	720 (C_{60})
$''m$[mg]$''$	6.7	39.7	5.0
$''C_{spin}''$	1.5 ppm	1	400 ppm
I_{sgn}	$3.7 \cdot 10^{-3}$	2964	$1.8 \cdot 10^{-4}$
V_{mod} [mV]	20	30	20
P_{mw} [mW]	1	10	1

Table 1: Parameters for filling efficiency, $''S(S+1)''$ effective value in the Curie susceptibility, M_{mol} is the molar weight of the medium, m is the weight of the sample, C_{spin} is the concentration of spins in the medium, I_{sgn} is the integrated signal intensity see (4.1), V_{mod} is the amplitude of the voltage in the modulation coils, P_{mw} is the power of the incident microwave on the sample

4.2 N@C_{60} hyperfine splitting

Here we describe the details of the ESR spectra of N@C_{60} peapod.

The ESR spectra of N@C_{60} on Fig. 4.1 shows the triplet lines characteristic to the endohedral atomic nitrogen. The 99.6% of natural nitrogen is ^{14}N of which has a $I = 1$ nuclear spin. $2I + 1$ gives the multiplicity of the lines which is in agreement with experiments. Because of the high symmetry of the C_{60} cage the encapsulated nitrogen can rotate freely that cancels out the off diagonal elements of the hyperfine tensor.

$$\mathbf{A}_{ISO} = A\mathbb{1} \tag{4.2}$$

The origin of the 3 absorption lines can be seen on Fig. 4.2. The 3 transitions which marked with the same line symbols coincide energetically, the small difference can be observed in spin-echo ESR experiments only [30]. The energy difference between $\langle S, m_S|\langle I, m_I|$ and $\langle S, m_S \pm 1|\langle I, m_I|$ states is due to the crystal field, which is small in case of C_{60} because of the high symmetry of the fullerene cage.

The electron spins interacts with the ^{13}C nuclear spins as well, but it can be neglected. The cwESR spectra of N@C_{60} does not show the characteristic hyperfine splitting of ^{13} due to the small overlap of the electron's wave function with the ^{13}C nuclei on the cage and the small natural abundance (every second C_{60} contains one ^{13}C).

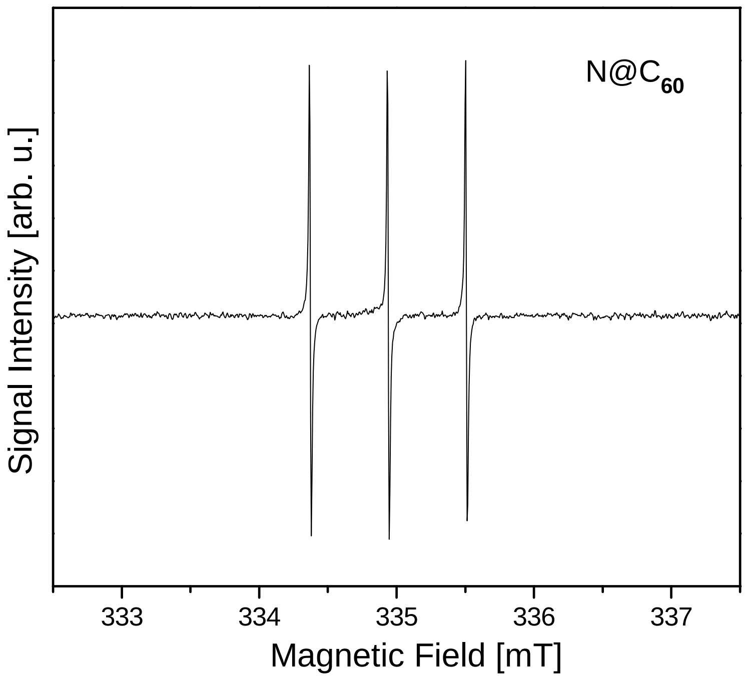

Fig. 4.1: ESR spectra of N@C$_{60}$ at room temperature

The temperature dependence of the isotropic hyperfine splitting of N@C$_{60}$ is shown in Fig. 4.3. The room temperature data for the peapod material is omitted, because the spectrometer had to be retuned for the 300 K measurement, that modifies the MW frequency. The large value of the hyperfine splitting is due to the compression of the electronic wave function inside the fullerene cage that increase the probability of finding the electron in the core the value of $|\psi(0)|^2$. At low temperatures ($T < 20$ K) the hyperfine coupling is constant, at higher temperature it increases. Assuming that the motion of the nitrogen atom inside the C$_{60}$ cage is like 3 dimensional harmonic oscillator and that the hyperfine coupling constant A linearly depends on the mean square displacement, the results can be correctly reproduced. At low temperature, the nitrogen atom is in its vibrational ground state making A constant, at higher temperature vibrational states are excited. At higher excited state, the mean amplitude is higher, thus the average distance of the nucleus and the outer shell electrons is smaller [32] increasing the hyperfine coupling. In case of three dimensional harmonic oscillator the Hamiltonian is

$$\mathcal{H}_{OSC} = \frac{\mathbf{p}^2}{2m} + \frac{1}{2} m\omega_0^2 \cdot \mathbf{r}^2 \,, \tag{4.3}$$

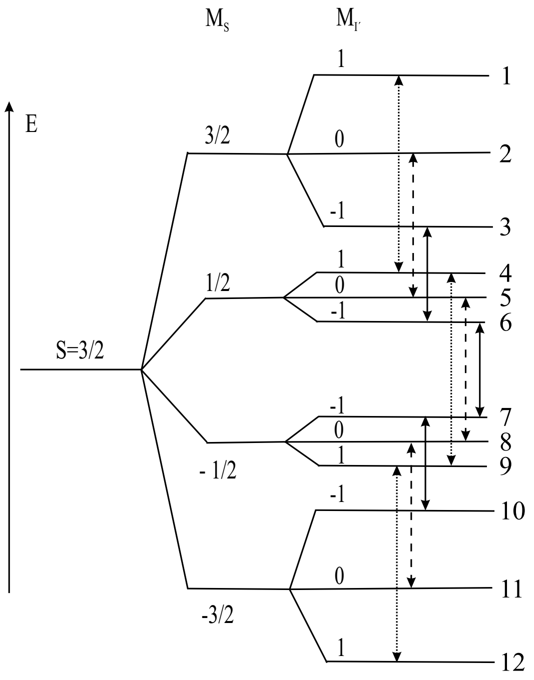

Fig. 4.2: Energy-level scheme for ^{14}N ($S = 3/2, I = 1$) in an external magnetic field (high-field limit). M_S and M_I are the electronic and nuclear spin quantum numbers, respectively. The vertical lines show the allowed ESR transitions, the three transitions (marked with the same line symbols) always coincide energetically, due to the negligible zero-field splitting [29].

whose eigenvalues are ($n = n_x + n_y + n_z$)

$$E_n = \hbar\omega_0 \left(n + \frac{3}{2}\right) . \tag{4.4}$$

The nth level degeneracy is $\frac{1}{2}(n+1)(n+2)$. A depends on the n quantum number

$$A(n) = \tilde{A}_0 + \Delta A \left(n + \frac{3}{2}\right) . \tag{4.5}$$

Assuming a Boltzmann distribution for the population of the excited vibrational states, the possibility of being found the system in the nth energy state is

$$P_n(T) = \frac{(n+1)(n+2)\exp\left(-\frac{n\hbar\omega_0}{k_B T}\right)}{\sum\limits_{n=0}^{\infty}(n+1)(n+2)\exp\left(-\frac{n\hbar\omega_0}{k_B T}\right)} . \tag{4.6}$$

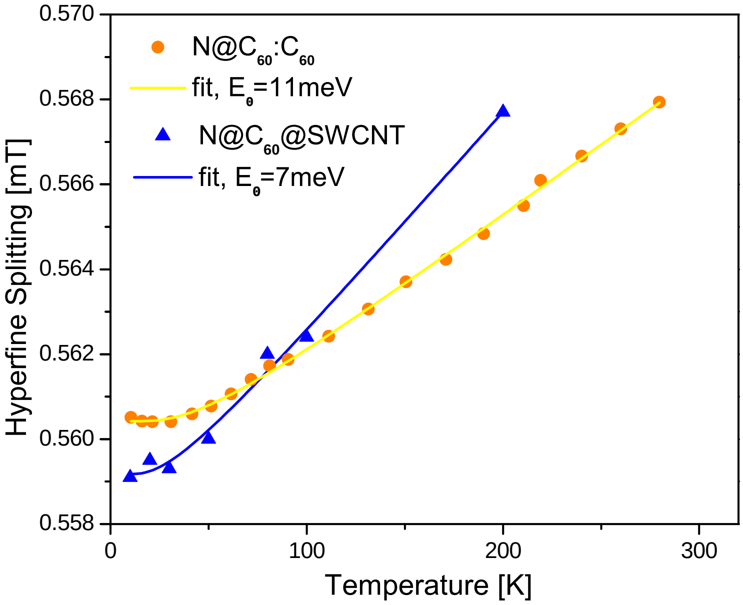

Fig. 4.3: Temperature dependence of hyperfine splitting, N@C$_{60}$:C$_{60}$ crystalline sample values from [31], N@C$_{60}$@SWCNT sample measured by F. Simon, the solid lines are fit with theoretical function, assuming that hyperfine coupling modified by vibrational excited states

$A(T)$ is the ensemble average of A

$$A(T) = P_n(T) \cdot A(n) = A_0 + \Delta A \frac{3}{\exp\left(\frac{\hbar\omega_0}{k_B T}\right) - 1}, \tag{4.7}$$

with $A_0 = \tilde{A}_0 + 3/2\Delta A$. Authors in Ref. [33] proposed a more sophisticated model, in which A is proportional to the mean square displacement to the power of $c = 0.85$ but this gives relevant difference only at temperatures higher than 300 K.

If N@C$_{60}$ is in crystalline form, the experimental $A(T)$ values can be fitted well with (4.7), which yields $\hbar\omega_0 = 11 \pm 2$ meV for the first excited energy, but using the model in [33] A. Weidinger *et al.* in [29] gained $\hbar\omega_0 = 18 \pm 1$ meV. In case of N@C$_{60}$@SWCNT sample the fit of the data yields an oscillator energy of $\hbar\omega_0 = 7 \pm 2$ meV. It has to be noted that although on Fig. 4.3 the difference between two ticks on the vertical axis is 1 μT which can be beyond the accuracy of the microwave frequency or the Hall effect sensor, the above results depends on the linearity of the magnetic field scale. Scaling or shifting the magnetic field does not effect the yielded value of oscillator energy.

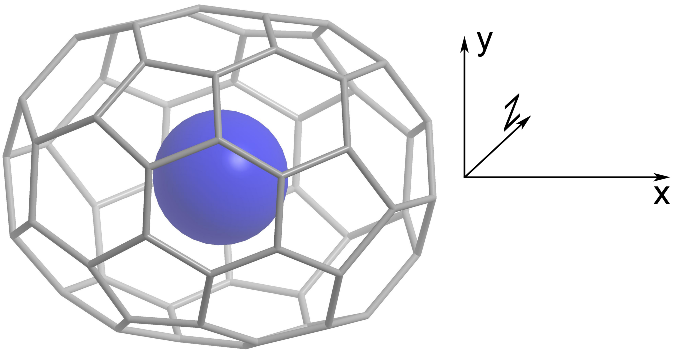

Fig. 4.4: The distorted fullerene molecule, the blue dot is nitrogen atom, surrounding nanotube not shown

The reason of different oscillator energy when N@C$_{60}$ is filled inside SWCNT is that nanotubes can distort the icosahedral symmetry of C$_{60}$ (see Fig. 4.4). Assuming that the fullerene molecule is stretched along the axis of the nanotube (let's call it x axis) and compressed in the perpendicular plane (y and z axes), the oscillator energy become smaller along the rotational symmetry axis of the fullerene and greater in the other two direction (x, y axes). At low temperature we can neglect excitations in the y-z plane, the vibration become one dimensional. $A(T)$ in this simple model, using the same argument as in three dimensional motion

$$A(T)_{1D} = A_0 + \Delta A \frac{1}{\exp\left(\frac{\hbar\omega_0}{k_B T}\right) - 1}, \tag{4.8}$$

where $A_0 = \tilde{A}_0 + 1/2\Delta A$. The fit of N@C$_{60}$@SWCNT data with this function yields the same oscillator energy of $\hbar\omega_0 = 7 \pm 2$ meV. To determine the oscillator energy in the y-z plane a more complicated analysis is needed, but lack of sufficient number of data points prevent such analysis.

4.3 Thermal stability of $N@C_{60}@SWCNT$

Waiblinger *et al.* [20] found that high temperature ($T > 500$ K) irreversibly destroys the molecule by the escape of the nitrogen. It is useful to compare the thermal stability of N@C$_{60}$ peapod with it.

To study the escape of nitrogen from N@C$_{60}$ at high temperature, we used a gas-flow insert for the Bruker spectrometer, which allows to control the temperature of the sample between 300 K and 620 K and to measure

ESR spectra simultaneously. The insert contains an electric heater and a thermoelectric thermometer. The heating media is nitrogen gas, which comes from a nitrogen tank and flows through the heater and through the resonant cavity which contains the sample. To reduce the temperature difference between the thermometer and the sample, the thermometer located as close to the sample as possible.

To compare our results with previous measurements, we follow the same temperature protocol, as used in Ref. [20]. This means we increased the temperature of the sample from 300 K at a speed of 45 s/K. The speed is very important because the escape mechanism of the nitrogen is a temperature activated process, so it is not a phase transition. At any temperature, the number of N@C_{60} decrease exponentially with time, only the decay rate changes with temperature. We record ESR spectra of our sample at every 2 K.

The ESR spectra of the crystalline sample (see Fig. 4.5) has a high noise ratio, it is due to the fact that time is limited to 90 s for every spectra. The spectra of the peapod sample contains a broad background line due to the presence of ferromagnetic Y:Ni nanoparticles, for comparison of the intensities see Fig 4.6. To determine the number of N@C_{60} , we fitted the baseline corrected spectra with 3 equidistant derivative Lorentzian functions. The sum of the intensity of the 3 lines is proportional to the Curie susceptibility of the sample since we use adequate power to be in the non saturating limit

$$I(T) \propto \chi_0 N(T) \propto \frac{1}{T} \cdot N(T)\,, \tag{4.9}$$

where $N(T)$ is the number of spins at unit volume. We observe a clear drop in the number of N@C_{60} in the crystalline material above ~ 550 K. However it is 50 K higher temperature than found in Ref. [20] and the decay is less sharp. We have no clear explanation for the difference. We believe that our temperature measurement is accurate. To check the result we made ex-situ measurements. We annealed the sample in a furnace outside of the ESR spectrometer every step involves a 10 minute annealing and an ESR measurement, we increased the temperature of the furnace after every step with 20 K. This gives results similar to the in-situ method.

The number of N@C_{60} in peapod decays much slower than in the crystalline material. At 620 K the relative $N(T)/N(400\text{ K})$ number of N@C_{60} is three times as much in peapod as in crystalline, the difference can be clearly seen in Fig. 4.5. The other difference is that the peapod sample starts to decay at 500 K earlier than the crystalline but the large noise of the

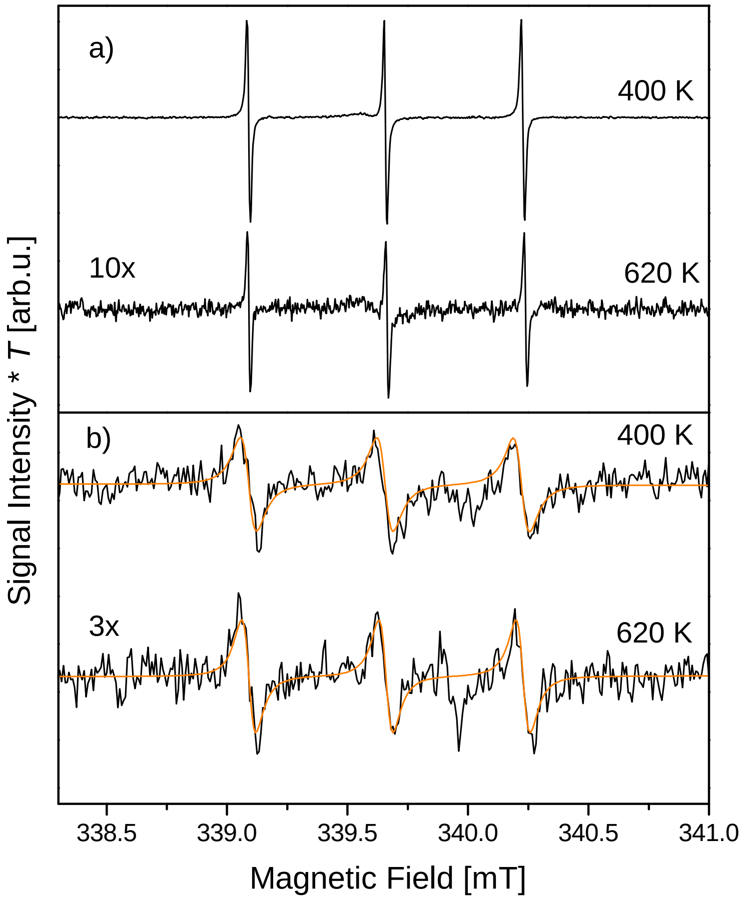

Fig. 4.5: ESR spectra of the a) crystalline and b) peapod samples multiplied by the temperature. The scale of the high temperature data are different for the two materials. Orange solid curves are the fitted Lorentzians to the data.

data makes it uncertain. The larger fluctuations are due to the dissipation of the microwave by the nanotube bundles.

The explanation for the stability of the peapod can be geometrical. The fullerene-fullerene distance in peapod is 0.97 nm. Is is between the lattice constant of the crystalline form of fullerene 1.002 nm [34] and of the polymerized fullerene 0.961 nm [35]. The voids between adjacent fullerenes are definitely smaller in peapod than in crystalline, this can geometrically prevent the nitrogen from swinging out. The available space around the fullerenes inside nanotube depends on the diameter of the tube, the Gaussian distribution of the diameter of the nanotubes can be the explanation for the smoothed decay of the number of N@C_{60} versus temperature.

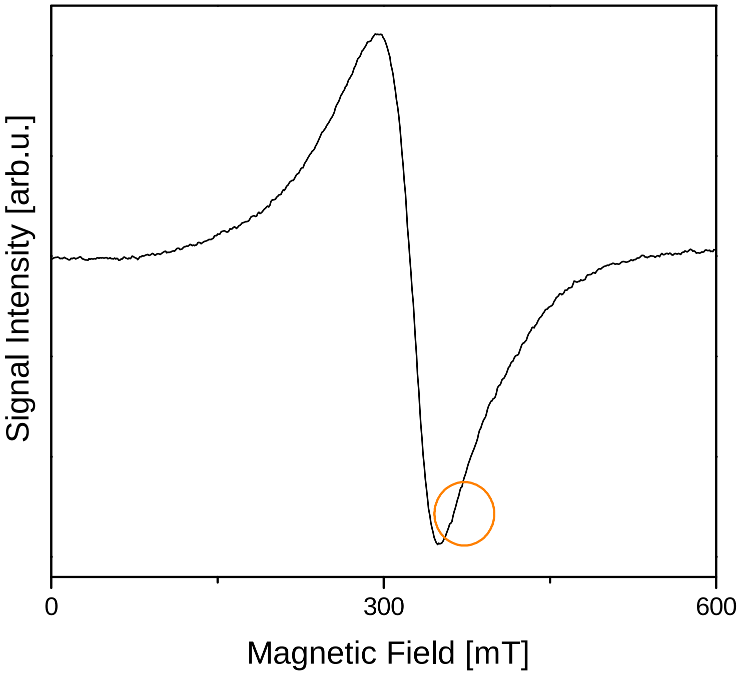

Fig. 4.6: ESR spectra of the peapod sample, in the orange circle the little kink is the triplet line of endohedral nitrogen.

4.4 Saturation measurement on $N@C_{60}@SWCNT$

The interaction between the N@C_{60} and host nanotube can modify the T_1 spin-lattice relaxation time of the endohedral nitrogen atom. We expect shortening of T_1 since the host nanotube lowers the symmetry of the fullerene cage, thus stronger interaction is expected between the endohedral nitrogen and the cage. To measure T_1 the most effective method is pulsed ESR, which allows to determine T_1 and T_2 independently. However, cwESR is suitable for that purpose as well with the limitation that we have to know one of them. The method is based on the measurement of the integrated susceptibility against microwave power and the fit of the measured curve with (2.27) yields $T_1 \cdot T_2$.

The T_2 spin-spin relaxation time is due to the dipolar interaction of like spins. In case of cubic lattice, the linewidth of the absorption signal reads [37]

$$\overline{\Delta B^2} = 24 \left(\frac{\mu_0}{4\pi}\right)^2 \gamma_e^2 \hbar^2 S(S+1) \frac{1}{d^6}\,, \tag{4.10}$$

where $\overline{\Delta B^2}$ is the second moment of the absorption signal, d is the lattice

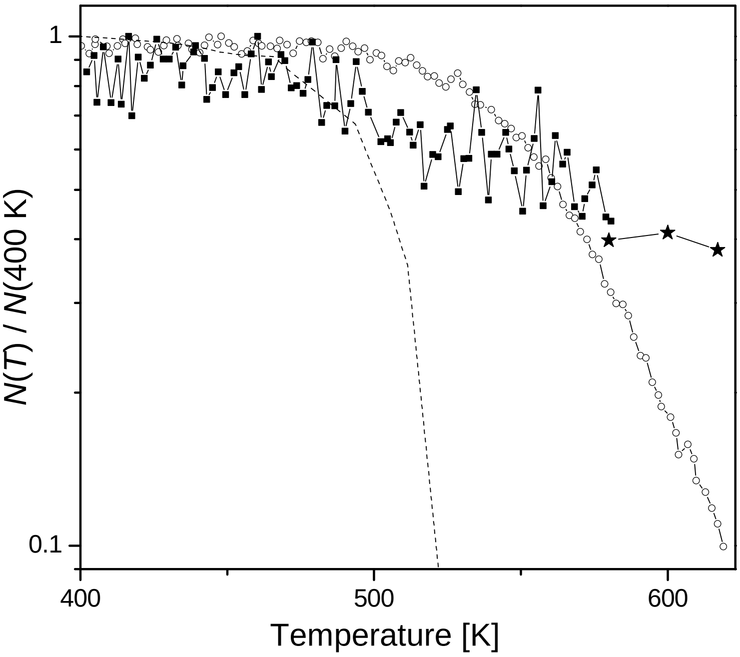

Fig. 4.7: Temperature dependence of the number of N@C_{60} . ○: crystalline, ■: peapod, ★: 5 times longer averaged data for peapod, dashed curve previous measurement on crystalline material from [20]

constant. T_2 can be calculated from the linewidth

$$T_2 = \frac{2\pi}{\sqrt{\overline{\Delta B^2}}} = \frac{4\pi^2 d^3}{\mu_0 \gamma_e^2 \hbar \sqrt{6S(S+1)}} . \tag{4.11}$$

If not every fullerene contains spins, the lattice constant can be substituted with the average distance between two spins that depends on the concentration

$$d_{avg}^3 = d^3/c\,, \tag{4.12}$$

where c is the concentration of N@C_{60} . In our sample the concentration of N@C_{60} is 400 ppm, the fullerene-fullerene distance is 1 nm, the calculated

	T_1 [µs]	T_2 [µs]
crystalline	120	5
peapod	13	13

Table 2: Relaxation times for N@C_{60} . Data for crystalline is taken from [36] with correction of T_2 (see text), relaxation times of peapod yielded from fit to measured saturation curve.

spin-spin relaxation time is T_2=5.1 μs. It is in good agreement with the measured value by pulsed ESR [36].

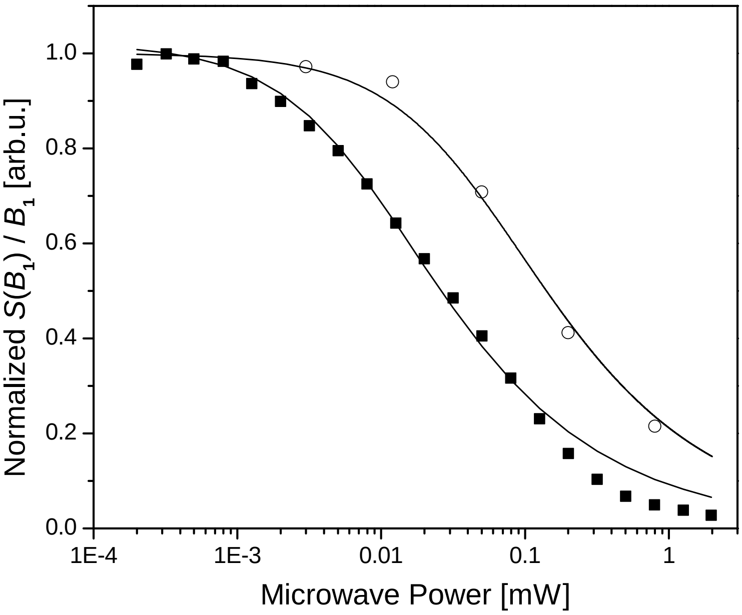

Fig. 4.8: Saturation curves for peapod (○) and crystalline (■) materials. The vertical axes correspond to the integrated χ'' divided by B_1 and normalized to the values at the lowest power. Solid curves are calculated saturated curves with parameter given in Table 2.

From T_1 and T_2 values of our crystalline material and using (2.63) we can simulate the saturation curve shown in Fig. 4.8, the quality factor of the cavity with the crystalline sample was Q = 3000. The simulated and measured curves fit well, that justifies the use of the saturated ESR method.

The quality factor of the cavity with the peapod sample was Q = 2000, the fit to the measured data yields T_1 and T_2 shown in Table 2. The two times are equal, because T_1 is so short, that it limits the value of T_2. The T_2 arose from dipolar interaction would be ~ 250 μs. The spin-lattice relaxation time of peapod material is shorter than the crystalline with a factor of 10, indicating new more effective relaxation route that the hyperfine relaxation [32][38]. We suggest that the lowered symmetry and modified electronic structure of N@C$_{60}$ is responsible for this.

5 Summary

In summary we studied the properties of the N@C60 magnetic fullerene when it is encapsulated inside single-walled carbon nanotubes using electron spin resonance spectroscopy.

We determined the concentration of N@C_{60} filled inside SWCNTs. We define the 100% filling factor as every nanotube is filled with tightly packed fullerenes. Using this definition we measured filling factor of 2%. The measurement of the number of N@C_{60} based on the microwave absorption. But inside the conductive nanotube bundles, the spins can be invisible for ESR because of the skin effect. Thus, the 2% is a lower estimate.

We studied the temperature dependence of hyperfine splitting in N@C_{60}@SWCNT . Following the literature model, we assume that the vibration of the N inside the C_{60} cage modifies the hyperfine splitting and the vibration of the nitrogen can be modelled with a quantum harmonic oscillator. This model is in a good agreement with our experimental results. The fit to the measured data yields an oscillator energy of 7 meV. In crystalline material the oscillator energy of 13 meV was reported. The lower energy in case of peapod material can be explained by the mechanical distortion of C_{60} .

We measured the thermal stability of N@C_{60} filled inside SWCNTs. The results show that the thermal stability of N@C_{60} is increased inside SWCNT. At 620 K the concentration of spins in N@C_{60}@SWCNT is 3 times higher than in crystalline material. Nanotubes can block the "swing out" process of the endohedral nitrogen, which explains the increased stability.

Finally, we determined the T_1 relaxation time of N@C_{60} filled inside SWCNT at room temperature. We used the saturation method to determine $T_1 \cdot T_2$ and with theoretically calculated T_2, we can determine T_1. The yielded T_1 is 10 times shorter than in crystalline N@C_{60} . The lowered symmetry and modified electronic structure of N@C_{60} can be responsible for this.

Most of these results are being published (Toth et al. Physical Review B, accepted for publication, in press, and Toth et al. Physica Status Solidi B, accepted for publication, in press). We believe that the results contribute to the exciting field of carbon nanotubes, however much additional work is required to fully exploit their application potential.

References

[1] S. Iijima and T. Ichihashi. Single-shell carbon nanotubes of 1-nm diameter. *Nature*, 363:603–605, 1993.

[2] E. Kymakis and G. A. J. Amaratunga. Single-wall carbon nanotube/conjugated polymer photovoltaic devices. *Applied Physics Letters*, 80:112–114, 2002.

[3] Walt A. de Heer, A. Châtelain, and D. Ugarte. A Carbon Nanotube Field-Emission Electron Source. *Science*, 270(5239):1179–1180, 1995.

[4] N. Pugno. On the strength of the nanotube-based space elevator cable: from nanomechanics to megamechanics. *Journal of physics. condensed matter*, 18:1971, 2006.

[5] B. W. Smith, M. Monthioux, and D. E. Luzzi. Encapsulated C_{60} in carbon nanotubes. *Nature*, 396:323–324, 1998.

[6] T. Shimada, T. Okazaki, R. Taniguchi, T. Sugai, H. Shinohara, K. Suenaga, Y. Ohno, S. Mizuno, S. Kishimoto, and T. Mizutani. Ambipolar field-effect transistor behavior of Gd@C_{82} metallofullerene peapods. *Appl. Phys. Lett.*, 81:4067–4069, 2002.

[7] F. Simon, H. Kuzmany, H. Rauf, T. Pichler, J. Bernardi, H. Peterlik, L. Korecz, F. Fülöp, and A. Jánossy. Low temperature fullerene encapsulation in single wall carbon nanotubes: synthesis of N@C_{60}@SWCNT. *Chem. Phys. Lett.*, 383:362–367, 2004.

[8] F. Simon, H. Kuzmany, B. Náfrádi, T. Fehér, L. Forró, F. Fülöp, A. Jánossy, A. Rockenbauer, L. Korecz, F. Hauke, and A. Hirsch. Magnetic fullerenes inside single-wall carbon nanotubes. *Phys. Rev. Lett.*, 97:136801–1–4, 2006.

[9] S. Tóth, D. Quintavalle, B. Náfrádi, L. Korecz, L. Forró, and F. Simon. Enhanced thermal stability and spin-lattice relaxation rate of N@C_{60} inside carbon nanotubes. *Physical Review B*, 77, 2008. In press.

[10] C. P. Slichter. *Principles of magnetic resonance*. Springer-Verlag, 1978.

[11] F. Bloch. Nuclear induction. *Phys. Rev.*, 70(7-8):460–474, Oct 1946.

[12] J. Sólyom. *A modern sziliárdtestfizika alapjai III.* ELTE Eötvös Kiadó, 2003.

[13] C. P. Poole. *Electron Spin Resonance*. John Wiley & Sons, New York, 1967 edition, 1967.

[14] A. M. Portis. Electronic structure of *f* centers: Saturation of the electron spin resonance. *Phys. Rev.*, 91(5):1071–1078, 1953.

[15] J. D. Jackson. *Klasszikus elektrodinamika*. Typotex, 2004.

[16] H. W. Kroto, J. R. Heath, S. C. O'Brien, R. F. Curl, and R. E. Smalley. C_{60}: Buckminsterfullerene. *Nature*, 318:162–163, 1985.

[17] T. Almeida Murphy, Th. Pawlik, A. Weidinger, M. Höhne, R. Alcala, and J.-M. Spaeth. Observation of atomlike nitrogen in nitrogen-implanted solid *c*60. *Phys. Rev. Lett.*, 77(6):1075–1078, Aug 1996.

[18] H. Mauser, A. Hirsch, N. Hommes, T. Clark, B. Pietzak, A. Weidinger, and L. Dunsch. Stabilization of atomic nitrogen inside C_{60}. *Angewandte Chemie*, 36(24):2835–2838, 1997.

[19] Greer J.C. The atomic nature of endohedrally encapsulated nitrogen N@C_{60} studied by density functional and hartree-fock methods. *Chemical Physics Letters*, 326:567–572(6), 25 August 2000.

[20] M. Waiblinger, K. Lips, W. Harneit, A. Weidinger, E. Dietel, and A. Hirsch. Thermal stability of the endohedral fullerenes N@C_{60}, N@C_{70}, and P@C_{60}. *Phys. Rev. B*, 64:159901–1–4, 2001.

[21] V. N. Bezmel'nitsyn, A. V. Eletskii, and M. V. Okun'. Fullerenes in solutions. *Physics-Uspekhi*, 41(11):1091–1114, 1998.

[22] `http://www.nanocarblab.com`.

[23] S. Iijima. Helical microtubules of graphitic carbon. *Nature*, 354:56–58, 1991.

[24] S. Reich, C.n Thomsen, and J. Maultzsch. *Carbon Nanotubes*. Wiley-VCH, 2004.

[25] Z. Shi, Y. Lian, X. Zhou, Z. Gu, Y. Zhang, S. Iijima, L. Zhou, K.T. Yue, and S. Zhang. Mass-production of single-wall carbon nanotubes by arc discharge method. *Carbon*, 37:1449–1453(5), 1999.

[26] F. Simon. Studying carbon nanotubes through encapsulation: from optical methods till magnetic resonance. *J. Nanosci. and Nanotechn.*, 7:1197–1220, 2007.

[27] K. Hirahara, S. Bandow, K. Suenaga, H. Kato, T. Okazaki, H. Shinohara, and S. Iijima. Electron diffraction study of one-dimensional crystals of fullerenes. *Phys. Rev. B*, 64(11):115420, Aug 2001.

[28] M. Melle-Franco, H. Kuzmany, and F. Zerbetto. Mechanical interaction in all-carbon peapods. *J. Phys. Chem. B*, 109:6986–6990, 2003.

[29] A. Weidinger, M. Waiblinger, B. Pietzak, and T. Almeida Murphy. Atomic nitrogen in N@C_{60}:C_{60}. *Applied Physics A*, 66:287–292, 1998.

[30] N. Weiden, H. Käß, and K. P. Dinse. Pulse electron paramagnetic resonance (EPR) and electron-nuclear double resonance (ENDOR) investigation of N@C_{60} in polycrystalline C_{60}. *J. Phys. Chem. B*, 103:9826, 1999.

[31] M. Waiblinger. *Untersuchungen der endohedralen Fullerene mit eingeschlossenen Stickstoff- und Phosphor-Atomen*. PhD thesis, Univerzität Konstanz, 2001.

[32] C. Meyer. *Endohedral Fullerenes for Quantum Computing*. PhD thesis, Freie Universitt Berlin, 2003.

[33] A. Grupp, B. Pietzak, M. Waiblinger, T. Almeida Murphy, A. Weidinger, and E. Roduner. Vibration of atomic nitrogen inside C_{60}. In *Proceedings of the international Winterschool on Electronic Properties of Novel Materials, Kirchberg, Austria*, 1997.

[34] P. A. Heiney, J. E. Fischer, A. R. McGhie, W. J. Romanow, A. M. Denenstein, J. P. McCauley Jr., A. B. Smith, and D. E. Cox. Orientational ordering transition in solid C_{60}. *Phys. Rev. Lett.*, 66(22):2911–2914, Jun 1991.

[35] Y. Iwasa, T. Arima, R. M. Fleming, T. Siegrist, O. Zhou, R. C. Haddon, L. J. Rothberg, K. B. Lyons, Jr. Carter, H. L., A. F. Hebard, R. Tycko, G. Dabbagh, J. J. Krajewski, G. A. Thomas, and T. Yagi. New Phases of C60 Synthesized at High Pressure. *Science*, 264(5165):1570–1572, 1994.

[36] W. Harneit. Fullerene-based electron-spin quantum computer. *Phys. Rev. A*, 65:032322, 2002.

[37] A. Abragam. *The principles of nuclear magnetism*. Clarendon Press, 1961.

[38] S. Knorr, A. Grupp, M. Mehring, M. Waiblinger, and A. Weidinger. Electron spin relaxation rates T_1 and T_2 in diluted solid N@C_{60}. *AIP Conf. Proc.*, 544:191–194, 2000.